


## Article

# Cyanogel-Induced Synthesis of RuPd Alloy Networks for High-Efficiency Formic Acid Oxidation

Qicheng Liu <sup>†</sup> , Wei Yan <sup>†</sup>, Jiachen Zhang, Yi Ren, Jiaqi Liu, Xin Zeng, Dongmei Sun <sup>\*</sup> and Yawen Tang <sup>\*</sup>

Jiangsu Key Laboratory of New Power Batteries, Jiangsu Collaborative Innovation Centre of Biomedical Functional Materials, School of Chemistry and Materials Science, Nanjing Normal University, Nanjing 210023, China

<sup>\*</sup> Correspondence: sundongmei@njnu.edu.cn (D.S.); tangyawen@njnu.edu.cn (Y.T.)

<sup>†</sup> These authors contributed equally to this work.

**Abstract:** For direct formic acid fuel cells (DFAFC), palladium (Pd)-based alloy catalysts with competitive morphology and elemental composition are essential to boost the performance of the formic acid oxidation reaction (FAOR) in the anode zone. Herein, we design and synthesize RuPd<sub>x</sub> alloy nano-network structures (ANs) via the facile wet-chemical reduction of Pd-Ru cyanogel (Pd<sub>x</sub>[Ru(CN)<sub>6</sub>]<sub>y</sub>·aH<sub>2</sub>O) as an effective electrocatalyst for the FAOR. The formation of Pd-Ru cyanogel depends on the facile coordination of K<sub>2</sub>PdCl<sub>4</sub> and K<sub>3</sub>[Ru(CN)<sub>6</sub>]. The unique structure of cyanogel ensures the presentation of a three-dimensional mesoporous morphology and the homogeneity of the elemental components. The as-prepared RuPd<sub>3</sub> ANs exhibit good electrocatalytic activity and stability for the FAOR. Notably, the RuPd<sub>3</sub> ANs achieve a mass-specific activity of 2068.4 mA mg<sup>-1</sup> in FAOR, which shows an improvement of approximately 16.9 times compared to Pd black. Such a competitive FAOR performance of RuPd<sub>3</sub> ANs can be attributed to the advantages of structure and composition, which facilitate the exposure of more active sites, accelerate mass/electron transfer rates, and promote gas escape from the catalyst layer, as well as enhance chemical stability.

**Keywords:** RuPd<sub>x</sub> alloy; cyanogel; nano-network; formic oxidation reaction



**Citation:** Liu, Q.; Yan, W.; Zhang, J.; Ren, Y.; Liu, J.; Zeng, X.; Sun, D.; Tang, Y. Cyanogel-Induced Synthesis of RuPd Alloy Networks for High-Efficiency Formic Acid Oxidation. *Catalysts* **2022**, *12*, 1136. <https://doi.org/10.3390/catal12101136>

Academic Editors: Orhan Şişman, Surjyakanta Rana, José Joaquín Velázquez García and Rajesh Dagupati

Received: 8 September 2022

Accepted: 25 September 2022

Published: 28 September 2022

**Publisher's Note:** MDPI stays neutral with regard to jurisdictional claims in published maps and institutional affiliations.



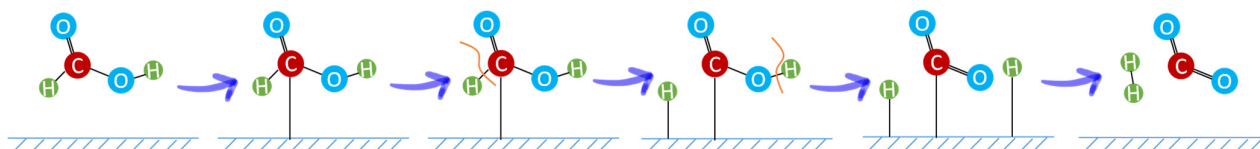
**Copyright:** © 2022 by the authors. Licensee MDPI, Basel, Switzerland. This article is an open access article distributed under the terms and conditions of the Creative Commons Attribution (CC BY) license (<https://creativecommons.org/licenses/by/4.0/>).

## 1. Introduction

Direct Formic Acid Fuel Cell (DFAFC) has been identified as a promising energy storage device by virtue of its low cost, high security, low-temperature adaptability, and theoretically large energy density [1–5]. Formic acid (HCOOH), as a fuel substance of DFAFC, is a clean and renewable energy source and can be obtained through biomass conversion processes [6–9]. As the anode reaction in a DFAFC, the formic acid oxidation reaction (FAOR, HCOOH → CO<sub>2</sub> + H<sub>2</sub>) performs an essential function in the energy density and charge/discharge cycle stability of the cell. Moreover, as a C1 molecular electrocatalytic reaction, FAOR has substantial research significance [10–12]. Pd-based materials are considered to be specific catalysts for the 2e<sup>-</sup> transfer step of FAOR in DFAFC (Scheme 1), possessing a lower polarisation potential and a more rapid kinetic step compared to the indirect pathway of Pt-based nanomaterials [13–15]. However, they have the following pressing problems. (1) Commercial Pd-based catalysts are expensive, [16] which limits the large-scale application of fuel cells [17]. (2) The FAOR performance of commercial catalysts is not yet sufficient and has considerable opportunities for improvement [18]. Accordingly, the design of catalysts with low cost and high activity/stability is a high priority for researchers [19–21].

The current strategies for enhancing the activity/stability of FAOR in Pd-based metal catalysts focus on electronic and structural modulation [22–24]. Electronic modulation is commonly utilized to enhance the intrinsic activity of catalysts [25–27]. The alloying/metallic of Pd with other 3d transition metals can achieve both cost reduction and modulation of the valence electrons in the Pd 3d orbitals [28], thus, improving the ability of

catalytic activity and anti-toxicity [29], Further, the alloying of Ru with Pd allows for superior resistance to  $\text{CO}_{\text{ads}}$  poisoning, while reducing the dosage of Pd metal. As a relatively inexpensive noble metal, Ru is only 1/5 the price of Pd. In previous research, alloying Ru with Pd has proven to be effective in improving these properties [30], because the -OH species generated on Ru can facilitate the oxidative removal of toxic intermediates, and the *d*-band centre of Pd will be shifted by Ru.



**Scheme 1.** The direct pathway involved in the HCOOH electrooxidation mechanism.

In terms of structural control, the architecture of the catalyst directly affects the exposition of the active site in the electrocatalytic reaction and the ability of the produced gas to escape [31,32], having a direct impact on the long-term stability and kinetic conversion efficiency of catalytic reactions, as well as causes the loss of mass transfer during DFAFC operation. Mesoporous-enriched three-dimensional (3D) materials typically have a large specific surface area and channels, which provides appreciable catalytically active sites and mass transport pathways in electrocatalytic reactions [33–35]. Moreover, large amounts of product gases are released during the DFAFC operation, whereas the 0 D structure does not facilitate the escape of  $\text{CO}_2$  and  $\text{H}_2$ , further avoiding the blocking of oxygen by the product gas under high current density. Pd-based alloy catalyst layers with 3D porous structures exhibit greater competitiveness than 0D, 1D and 2D nanomaterials when operating in DFAFC.

The cyanogel-induced synthesis of nanoelectrocatalysts can achieve a combination of these two advantages. The cyanogel-induced synthesis of Pd-based alloy catalysts has been demonstrated in previous studies [36], due to the special coordination pattern of cyanogel that allows the Pd and the other 3*d*-transition (M) atoms (such as Fe [37], Co [38], Ni [39–41], Rh [42], Pt [43] and Cu [44], etc.) to occupy specific positions along the cyanogel skeleton, thus, enabling a predictable morphological and electronic structure during liquid phase reduction, resulting in better long-term stability in electrochemical tests. In addition, the conditions for the synthesis of cyanogel are in line with the concept of low carbon emissions and environmental friendliness. The strategy results in a stable colloidal structure at ambient temperature and pressure. The reduction process is rapid, usually taking only a few seconds to obtain a phase homogeneous alloy, and the high feed conversion rate of the cyanogel reduction reaction results in almost eliminating feedstock waste, as well as allowing for high throughput production.

In this work, for the first time, a series of yellow, orange and tawny Ru-Pd-based cyanogels are conveniently available by using potassium chloropalladite ( $\text{K}_2\text{PdCl}_4$ ) and potassium hexacyanoruthenate ( $\text{K}_3[\text{Ru}(\text{CN})_6]$ ) as precursors. Notably, this is the first report on the usage of Ru-based cyano inorganic complexes for the synthesis of cyanogels. The molar ratio of Ru/Pd in the cyanogels can easily be adjusted by controlling the feeding ratios, and this feature of  $\text{Pd}_x[\text{Ru}(\text{CN})_6]_y \cdot a\text{H}_2\text{O}$  cyanogels facilitates the subsequent construction of alloy products with controllable compositions and adjustable properties. Ultimately, the  $\text{RuPd}_x$  alloy was successfully reduced by  $\text{NaBH}_4$ . The  $\text{RuPd}_3$  ANs exhibited superior catalytic activity and stability in the electrocatalytic FAOR (Scheme S1).

## 2. Results and Discussion

### 2.1. Physical Characterisation of $\text{Pd}_x[\text{Ru}(\text{CN})_6]_y \cdot a\text{H}_2\text{O}$ Cyanogels

As observed, the stable  $\text{Pd}_x[\text{Ru}(\text{CN})_6]_y \cdot a\text{H}_2\text{O}$  cyanogels can be obtained at a series of feeding ratios of  $\text{K}_2\text{PdCl}_4$  and  $\text{K}_3[\text{Ru}(\text{CN})_6]$  from 1:1, 2:1, and 3:1 (Figure S1). According to the principle of cyanogel formation, the ruthenium cyanide ion ( $[\text{Ru}(\text{CN})_6]^{3-}$ ) rapidly

coordinates with chloropalladite ion ( $[\text{PdCl}_4]^{2-}$ ) and forms a Ru-CN-Pd bond. The aurantiacus  $\text{Pd}_x[\text{Ru}(\text{CN})_6]_y \cdot a\text{H}_2\text{O}$  cyanogel is completed in an instant. The RuPd $_x$  alloy networks were grown on a cyanogel skeleton by using an excess of fresh aqueous  $\text{NaBH}_4$  solution as a reducing agent at room temperature.

The crystal structure of the prepared  $\text{Pd}_x[\text{Ru}(\text{CN})_6]_y \cdot a\text{H}_2\text{O}$  cyanogels were characterized by X-ray diffraction (XRD) tests (Figure 1a). The results show that  $\text{Pd}_x[\text{Ru}(\text{CN})_6]_y \cdot a\text{H}_2\text{O}$  cyanogels exhibit the amorphous peak shape of the classical Prussian-like structure in terms of crystal structure after freeze-drying into aero-cyanogels, which matches the peak positions of other Prussian-like structures reported in the previous research [45]. Furthermore, the series of peaks that are situated on 28.33, 40.49, 50.15, 58.60, 66.35 and 73.70 belong to the standard card KCl (JCPDS 97-015-4214), suggesting the by-product prefers to be KCl, rather than KCN, in the formation of the  $\text{Pd}_x[\text{Ru}(\text{CN})_6]_y \cdot a\text{H}_2\text{O}$  cyanogel:

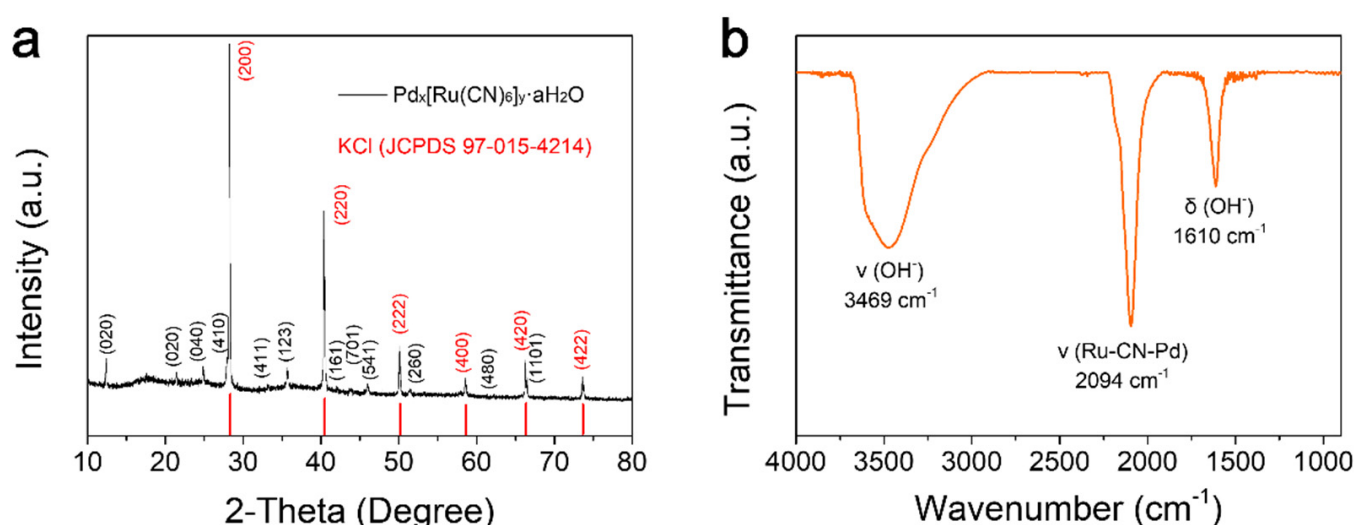
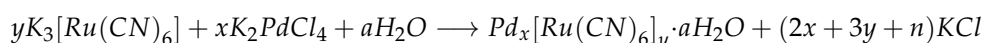


**Figure 1.** (a) X-ray diffraction (XRD) pattern and (b) Fourier transform infrared (FT-IR) spectrum of  $\text{Pd}_x[\text{Ru}(\text{CN})_6]_y \cdot a\text{H}_2\text{O}$  aero-cyanogel.

The coordination was further verified by the Fourier transform infrared (FT-IR) spectra (Figure 1b). The sharp peak, stretching the vibration peaks of the cyanogroup, at  $2096\text{ cm}^{-1}$ , indicates the formation of a Ru-CN-Pd bond, which further suggests that Ru is linked to Pd by a cyanogroup-bridging coordination [46]. The peaks at  $3469$  and  $1610\text{ cm}^{-1}$  belong to the hydroxyl stretching and bending vibrational peaks of crystallized water, respectively [44].

## 2.2. Physical Characterisation of As-Prepared RuPd $_3$ ANs, RuPd $_2$ and RuPd

The RuPd $_3$  ANs and contrast samples (RuPd $_2$  and RuPd) were obtained by a liquid-chemical reduction process, using fresh  $\text{NaBH}_4$  solution. The atomic content of Pd and Ru was confirmed by energy dispersive spectroscopy (EDS, Figure S3), consisting with the inductively coupled plasma mass spectrometry (ICP-MS) test results (Ru/Pd = 51.1/48.9, 35.4/64.6 and 23.2/76.8). Moreover, the elemental ratio of RuPd $_x$  is close to the feeding ratio in the preparative process, indicating that the catalyst prepared by the cyanogel method can achieve a high reaction conversion rate, as well as effectively avoiding the waste of noble metals in the synthetic process. As characterised by XRD patterns (Figure 2a), the 2-Theta diffraction peaks of RuPd $_3$  ANs situated on 39.71, 45.62 and 67.43 are attributed to the (111), (200) and (220) facets, respectively, which are between Pd (JCPDS 97-006-4914) and Ru (JCPDS 97-004-1515) standard cards, suggesting the formation of RuPd $_x$  alloy. Compared to RuPd $_2$  and RuPd, the diffraction peaks show a clear leftward shift between the Ru and Pd JCPDS cards, as well as towards the Pd side, which further demonstrates

that both Ru and Pd elemental ratios can be changed to form stable alloy phases rather than heterogeneous structures/interfaces. Clearly shown in Figure S2, the lattice parameter appeared on a straight fitted line based on a solid solution between Pd and Ru, in the light of Vegard's Law:  $d_{\text{RuPd}} = x \cdot d_{\text{Pd}} + (1 - x) \cdot d_{\text{Ru}}$ , confirming the well-defined alloy formation in RuPd<sub>3</sub> ANs.

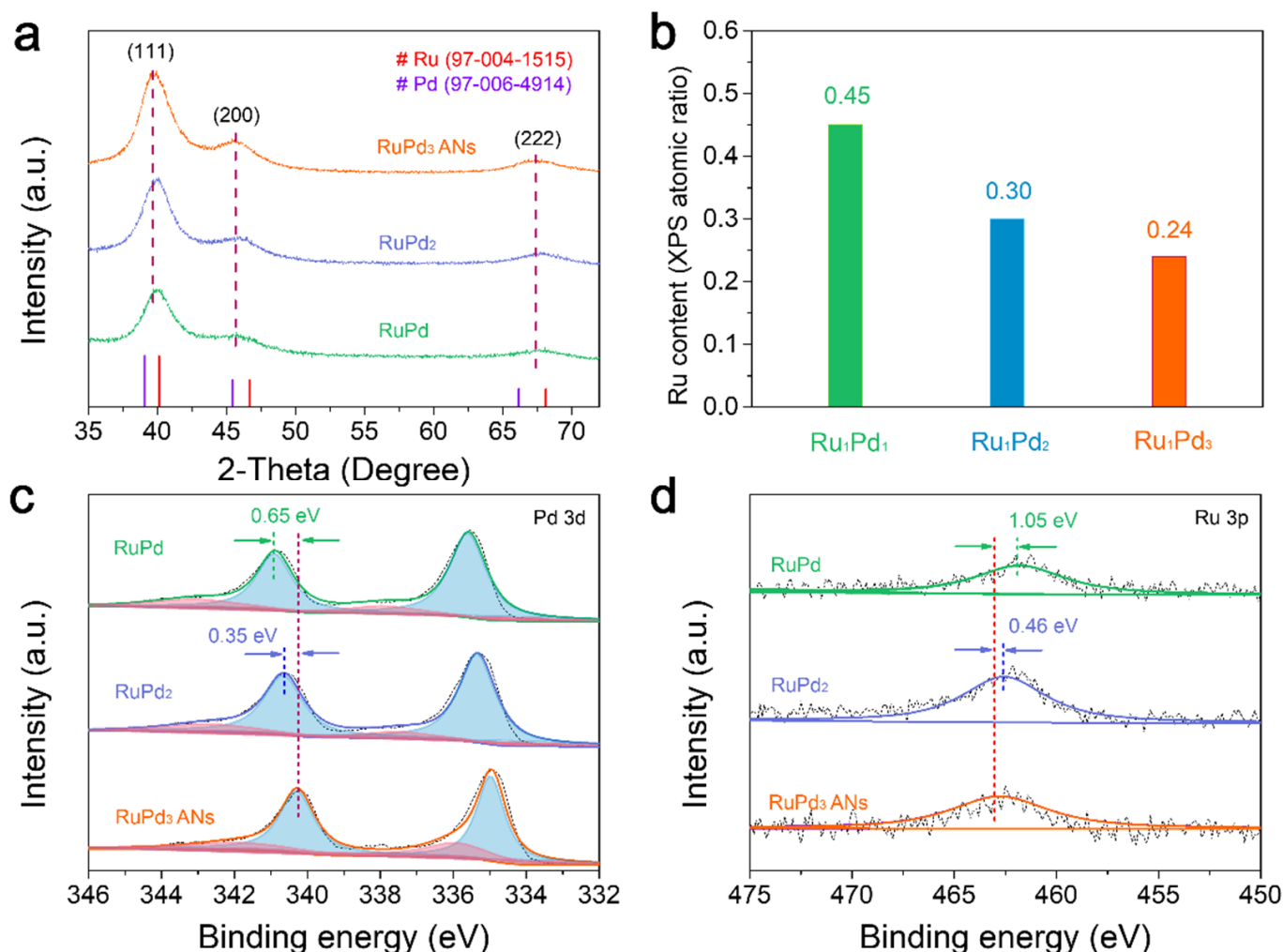


**Figure 2.** (a) XRD pattern; (b) X-ray photoelectron spectroscopy (XPS) spectrum of surface element ratio; (c) XPS spectrum of Pd 3d; and (d) Ru 3p for RuPd<sub>3</sub> ANs (Orange), RuPd<sub>2</sub> (Blue) and RuPd (Green).

Further, an XPS measurement (Figures 2b–d and S4) was performed to investigate the changes in the surface properties of the catalysts under different element ratios. According to the XPS analysis (Figure 2b), the surface ratios of Ru for RuPd<sub>3</sub>, RuPd<sub>2</sub> and RuPd are approximately 0.45, 0.30 and 0.24, respectively, which are consistent with the EDS and ICP results (Table 1), demonstrating that the cyanogel-induced synthesis of RuPd<sub>x</sub> alloys networks are all homogeneous physical phases rather than core-shell structures.

**Table 1.** The element analysis (Ru content) of RuPd, RuPd<sub>2</sub> and RuPd<sub>3</sub> ANs.

Sample Name	EDS Analysis	XPS Analysis	ICP Analysis
RuPd	0.47	0.45	0.51
RuPd <sub>2</sub>	0.30	0.30	0.35
RuPd <sub>3</sub>	0.12	0.24	0.23

Moreover, changes in elemental composition can also play a role in the modulation of the electronic structure of the alloy phase, as was demonstrated by comparing the Ru and Pd elemental binding energies of RuPd<sub>3</sub> ANs, RuPd<sub>2</sub> and RuPd. For RuPd<sub>3</sub> ANs, two peaks appeared at the binding energy of 334.94 and 340.24 eV, which were ascribed as Pd 3d<sub>5/2</sub> and Pd 3d<sub>3/2</sub>, respectively (Figure 2c), indicating the negative shift of 0.35 and 0.65 eV to a lower binding energy with respect to that of RuPd<sub>2</sub> and RuPd. It is implied by the reduction in binding energy that the electron donation from Ru to Pd and the *d*-band centre of Pd may be downward-shifted, which favours a weakening of the interaction between the Pd surface and the absorber, so as to boost the electrocatalytic activity in FAOR [28,47]. By contrast, the binding energy of Ru 3p is elevated, with the RuPd<sub>3</sub> ANs showing a 0.46 and 1.05 eV positive shift compared to RuPd<sub>2</sub> and RuPd, respectively (Figure 2d). In summary, with the increase in Pd content, the binding energy of Ru gradually increases, while Pd shows the opposite shift, further verifying that Ru has a significant modulating effect on the electronic structure of Pd and shows binding energy which is favourable to the electrocatalytic reaction of Pd-based materials at Ru/Pd = 1:3.

### 2.3. Microscopic Morphological Characterisation

The morphological and structural characterisation of as-prepared RuPd<sub>3</sub> ANs were achieved by a scanning electron microscope (SEM) and high-resolution transmission electron microscopy (HRTEM). The 3D porous structure of RuPd<sub>3</sub> ANs was confirmed by SEM (Figure S5). Confirmed by the magnified SEM (Figure 3a) and wide-ranged HRTEM images (Figure 3b), the nano-network structure incorporates abundant mesoporous channels, which provide more active sites for the FAOR as well as facilitate the escape of gases from the catalyst layer [45,48]. The surface area of the catalyst for RuPd<sub>3</sub> ANs was calculated by Brunauer–Emmett–Teller (BET) to be 245.78 m<sup>2</sup> g<sup>-1</sup> from the adsorption-desorption isotherm of N<sub>2</sub> (Figure S6a). The pore size distribution graph further confirms the porous structure of RuPd<sub>3</sub> ANs with a mesoporous pore size of approximately 4.8 nm (Figure S6b). As shown in Figure 3c, the further enlarged HRTEM image revealed clear lattice stripes, which further confirmed the well-crystallised quality of the RuPd<sub>3</sub> ANs. The lattice distance of RuPd<sub>3</sub> ANs measured by the HRTEM (Figure 3d) is 0.228 nm, which is between Pd (111) and Ru (111), consistent with results from XRD patterns. This further verified the Ru content to be approximately 25%. EDS elemental mapping shows a homogeneous distribution of Ru and Pd along the nano-network (Figure 3e), indirectly verifying the ordered arrangement of the RuPd<sub>3</sub> alloy formed on the basis of the cyanogel skeleton.

### 2.4. Electrochemical Analysis

Cyclic voltammetry tests of RuPd<sub>3</sub> ANs, RuPd<sub>2</sub>, RuPd and Pd black were carried out in a 0.5 M H<sub>2</sub>SO<sub>4</sub> aqueous solution to investigate their electrochemical properties (Figure S7). By calculating the oxygen reduction peak, the electrochemically active surface area (ECSA) of RuPd<sub>3</sub> ANs, RuPd<sub>2</sub>, RuPd and Pd black can be estimated to be 8.1, 7.3, 3.7 and 6.6 m<sup>2</sup> g<sup>-1</sup>, respectively (Figure 4a). The reduction peak potential on RuPd<sub>3</sub> ANs is negatively shifted by 56, 166 and 82 mV compared to that of RuPd<sub>2</sub>, RuPd and Pd black catalysts, respectively, indicating that RuPd<sub>3</sub> ANs can provide –OH species at a lower potential, which is conducive to the 2 e<sup>-</sup> transfer pathway of FAOR. It also provides further evidence that the elevated content of Ru/Pd = 1:3 is more conducive to the electrocatalytic FAOR. The electrocatalytic activities for the FAOR of these four catalysts were assessed by CV curves (Figure 4b,c) conducted in N<sub>2</sub>-saturated 0.5 M H<sub>2</sub>SO<sub>4</sub> + 0.5 M HCOOH at 50 mV s<sup>-1</sup>. Compared to the Pd black, both the RuPd<sub>3</sub> ANs and RuPd<sub>2</sub> take on much larger mass-normalized peak current densities for FAOR. The improved FAOR activities of these catalysts could be ascribed to the modification of the electronic structure, which is the reduction in the electronic density of states near the Fermi level. The RuPd<sub>3</sub> ANs exhibit superior mass electrocatalytic activity with a peak current density of 2068.4 mA mg<sub>Pd</sub><sup>-1</sup>, which was 2.9, 7.6 and 16.9 times higher than that of RuPd<sub>2</sub> (705.8 mA mg<sub>Pd</sub><sup>-1</sup>), RuPd (277.3 mA mg<sub>Pd</sub><sup>-1</sup>), and Pd black (122.2 mA mg<sub>Pd</sub><sup>-1</sup>), respectively. The FAOR mass

specific activity of RuPd<sub>3</sub> ANs is higher than most reported Pd-based electrocatalysts (Table S1), demonstrating that RuPd<sub>3</sub> ANs can achieve higher current densities at lower potentials. Moreover, compared to RuPd<sub>2</sub> and RuPd catalysts, RuPd<sub>3</sub> ANs have lower oxidation potentials for FAOR, with potential advantages of 77 and 222 mV, respectively. In the comparison of area specific activity, RuPd<sub>3</sub> ANs display 1.4 times the current density of Pd Black, as well as a negative shift of 82 mV of onset potential for FAOR, indicating that RuPd<sub>3</sub> ANs possess the best intrinsic activity. From the Tafel plots in Figure 4e, the RuPd<sub>3</sub> ANs present a higher output current density than RuPd<sub>2</sub>, RuPd and Pd black at the same polarization overpotential, suggesting favourable charge transfer and promoted reaction kinetics of FAOR. The electrochemical impedance spectroscopy (EIS) of RuPd<sub>3</sub> ANs and Pd black (Figure S8) shows that RuPd<sub>3</sub> ANs exhibit a smaller semi-circular arc in the region of kinetic control (high-frequency zone) than that of Pd black, which indicates that RuPd<sub>3</sub> ANs have less charge transfer resistance ( $R_{ct}$ ) than Pd black in acidic condition. The chronoamperometric measurements shown in Figure S9 were brought into effect in 0.5 M H<sub>2</sub>SO<sub>4</sub> + 0.5 M HCOOH electrolyte at a ceaseless potential of 0.6 V (vs. RHE). After 6000 s, commercial Pd black decreased to 0.4 mA cm<sup>-2</sup>, while the RuPd<sub>3</sub> ANs showed a comparative decrease of 40.13% to 15.1 mA cm<sup>-2</sup>. To further investigate the electrochemical behaviour of RuPd<sub>3</sub> ANs and Pd black during FAOR, 200 cycles of an accelerated endurance test (ADTs) were executed in 0.5 M H<sub>2</sub>SO<sub>4</sub> + 0.5 M HCOOH electrolyte. As shown in Figure S10a, with the increase in the CV cycles, the current density enhances slightly, and then gradually stabilizes after 60 cycles. Compared to the rapid decay of the Pd black counterpart (Figure S10b), RuPd<sub>3</sub> ANs exhibit better FAOR stability. Over the next 140 cycles of testing, both RuPd<sub>3</sub> ANs and Pd black all show varying degrees of attenuation. At 200th cycles, the mass-normalized activity of RuPd<sub>3</sub> ANs decays to 855.0 mA mg<sub>Pd</sub><sup>-1</sup> (41.35% of the current density in the first cycles), which is still 7.0 times higher than that of Pd black. The Pd black decays to 18.2 mA mg<sub>Pd</sub><sup>-1</sup> in the 200th cycle, which is only 14.9% of the current density in the first cycle. Notably, after 60 cycles of ADTs, the FAOR curve for Pd black showed two distinct oxidation peaks, suggesting an indirect pathway to electrocatalytic FAOR after the poisoning of Pd black, while that for RuPd<sub>3</sub> ANs maintained its initial electrochemical characteristics, suggesting a clear advantage of RuPd<sub>3</sub> ANs over Pd black in terms of their anti-CO toxicity performance. The morphology of the RuPd<sub>3</sub> ANs can be well maintained after ADTs testing. As shown in Figure S11, the morphology of RuPd<sub>3</sub> ANs was not significantly changed, and the mesoporous-enriched 3D structure did not collapse/agglomerate, benefiting from the structural stability derived from the robust cyanogel skeleton.

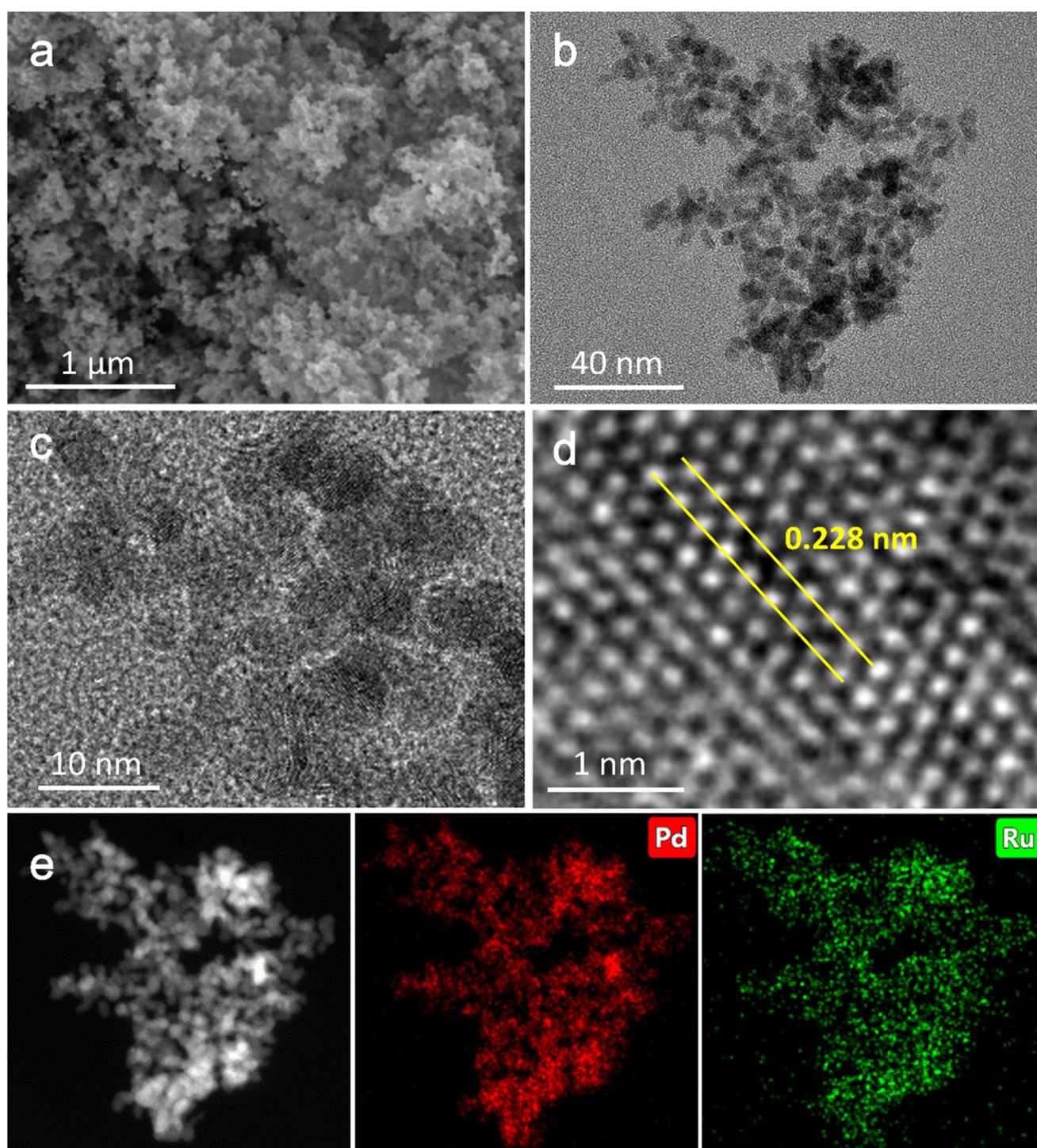


**Figure 3.** (a) Scanning electron microscope (SEM) image; (b–d) high-resolution transmission electron microscope (HRTEM) images of RuPd<sub>3</sub> ANs; (e) EDS mapping spectrum of RuPd<sub>3</sub> ANs.

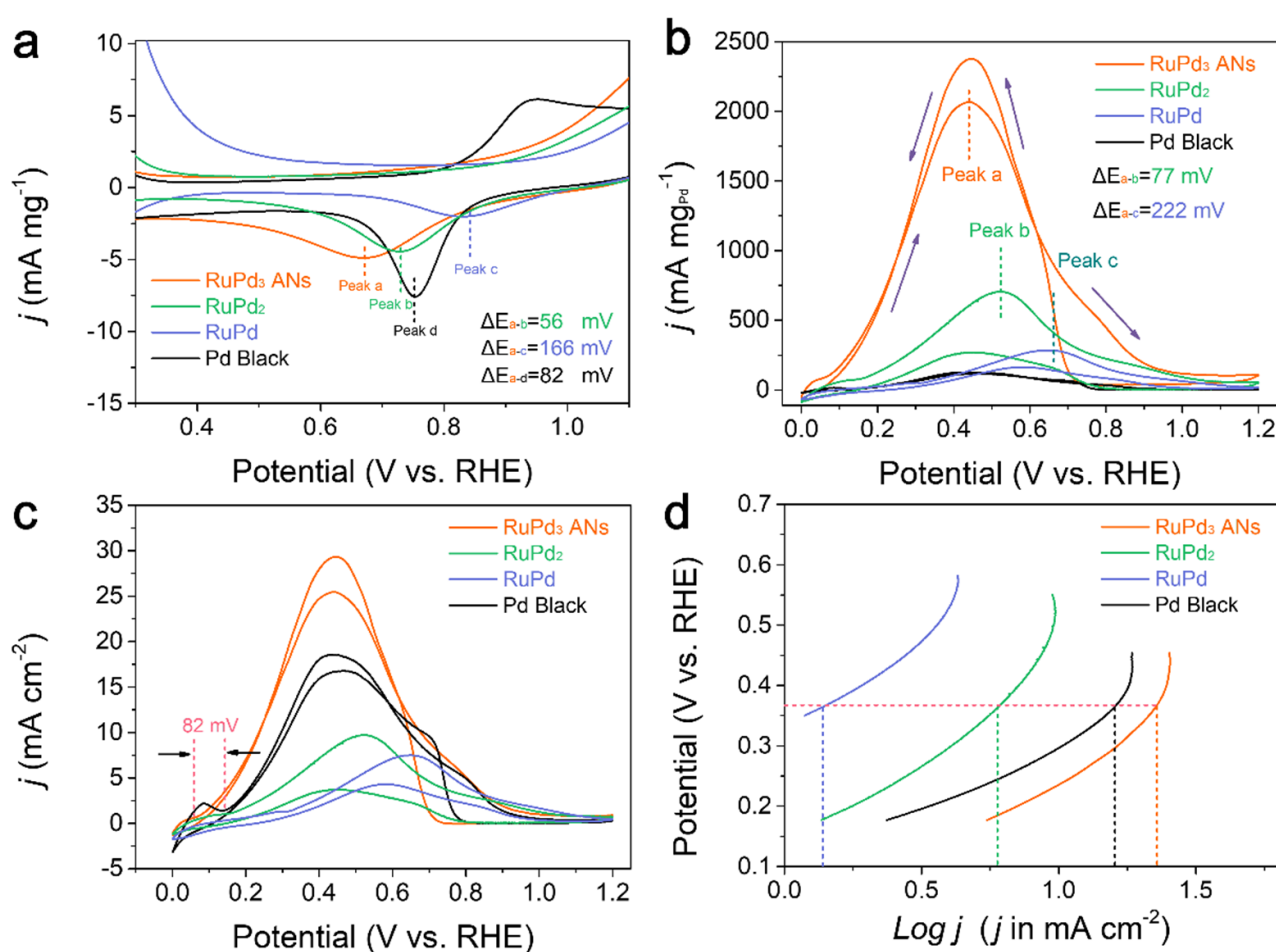


**Figure 4.** Comparison of the formic acid oxidation reaction (FAOR) performances of RuPd<sub>3</sub> ANs, RuPd<sub>2</sub>, RuPd and Pd black. (a) Cyclic voltammetry (CV) curves (enlarged image) in 0.5 M H<sub>2</sub>SO<sub>4</sub> solution; (b) mass-normalized and (c) area-normalized FAOR curves in N<sub>2</sub>-saturated 0.5 M H<sub>2</sub>SO<sub>4</sub> + 0.5 M HCOOH solution; (d) Tafel plots.

### 3. Materials and Methods

#### 3.1. Electrochemical Analysis

Potassium hexacyanoruthenate (K<sub>3</sub>[Ru(CN)<sub>6</sub>]) was supplied by Alfa Aesar Co., Ltd. (Shanghai, China). Potassium chloropalladite (K<sub>2</sub>PdCl<sub>4</sub>) was purchased from D.B. Chemical Reagent Co., Ltd. (Shanghai, China). Formic acid (HCOOH), ethanol (C<sub>2</sub>H<sub>5</sub>OH), sulfuric acid (H<sub>2</sub>SO<sub>4</sub>) and sodium borohydride (NaBH<sub>4</sub>) were purchased from Sinopharm Chemical Reagent Co., Ltd. (Shanghai, China). Pd black was purchased from Johnson Matthey Corporation. All the reagents were not further purified.

#### 3.2. Methods—Synthesis of RuPd<sub>x</sub> Alloy Networks

In a typical synthesis, K<sub>3</sub>[Ru(CN)<sub>6</sub>] solution (0.3 mL, 0.1 M) was added to K<sub>2</sub>PdCl<sub>4</sub> (0.3, 0.6 and 0.9 mL, 0.1 M) solution in continuous oscillation. Concussion should stop immediately after mixing. Pd<sub>x</sub>[Ru(CN)<sub>6</sub>]<sub>y</sub>·aH<sub>2</sub>O cyanogel quickly formed in a matter of minutes. Then, the newly prepared excess NaBH<sub>4</sub> (5.0 mL, 0.2 M) was added to Pd<sub>x</sub>[Ru(CN)<sub>6</sub>]<sub>y</sub>·aH<sub>2</sub>O cyanogel. After two hours, the black RuPd, RuPd<sub>2</sub> and RuPd<sub>3</sub> ANs were obtained by ultrasonic pulverisation in a cell pulveriser for 4 min, followed by centrifugal washing several times.

#### 3.3. Characterisation

High-resolution transmission electron microscopy (HRTEM) and HADDF-STEM images were obtained on the Talos F200x G2 microscope operated with an accelerating voltage



of 200 kV (Wuhan, China). The scanning electron microscopy (SEM) was characterized by Hitachi S4800 scanning electron microscopy (Nanjing, China). EDS measurements were conducted on Oxford Instruments ULTIM MAX 170 (Nanjing, China). The concentrations of metals were then measured with a Thermo Scientific Plasma Quad inductively coupled plasma mass spectrometry (ICP-MS, (Nanjing, China) and EDS (Nanjing, China). XPS measurements were conducted on a Thermo VG Scientific ESCALAB 250 spectrometer with an Al K $\alpha$  radiator (Zibo, China). The binding energy was calibrated by means of the C 1s peak energy of 284.6 eV. XRD analyses were performed on a Model D/max-rC X-ray diffractometer employing K $\alpha$  radiation ( $\lambda = 0.15406$  nm) (Nanjing, China). BET measurements were required on MicrotracBEL BELSORP-max (Zibo, China) with adsorptive of N<sub>2</sub>. The apparatus temperature and adsorption temperature are 0 °C and 77 K, respectively.

### 3.4. Electrochemical Measurements

Electrochemical measurements were performed on a CHI 760E analyser (Chenhua Co. Shanghai, China) with a conventional three-electrode system. The glassy carbon electrode loaded with catalyst was used as the working electrode, the graphite rod as the counter electrode, and the saturated calomel electrode (SCE) as the reference electrode for the FAOR tests. In electrochemical testing, 4.0 mg of electrocatalysts was dispersed into a mixture of 0.7 mL of alcohol, 1.2 mL of deionized water and 0.1 mL of Nafion solution (5 wt%), and the above substances were mixed by sonication thoroughly for 30 min. Then, 10  $\mu$ L of the acquired catalyst ink (2 mg mL<sup>-1</sup>) was dropped onto the surface of the glass carbon electrode of 3.0 mm in diameter. Thus, the mass loading of the catalyst on the GC electrode is 0.285 mg cm<sup>-2</sup>. The catalysts were pre-activated in a cyclic voltammetric window in 0.5 M H<sub>2</sub>SO<sub>4</sub> solution before the ADTs were tested.

## 4. Conclusions

In summary, we have developed a new strategy for the construction of Pd<sub>x</sub>[Ru(CN)<sub>6</sub>]<sub>y</sub>·aH<sub>2</sub>O cyanogels, using K<sub>3</sub> [Ru(CN)<sub>6</sub>] as metal salt precursors, by utilizing the principles of cyanogel synthesis, as well as RuPd<sub>x</sub> alloy network-like catalysts, which were further obtained at ambient temperature and pressure. During electrocatalytic FAOR testing, the RuPd<sub>3</sub> ANs catalyst demonstrated a competitive electrocatalytic mass/area specific activity, electron/proton transfer rates, and operational long-term stability in comparison to commercial Pd black catalyst and other element ratio component of RuPd<sub>x</sub> alloys (1:1 and 1:2). The competitive FAOR activity can be attributed to the advantage of a stable 3D nano-network structure, and the modulating effect of electronic effects due to the specific RuPd<sub>3</sub> component ratio. The RuPd<sub>3</sub> ANs show good prospects for the catalyst layer in DFAFC. In addition, this work provides guidance for the subsequent synthesis of cyanogels using ruthenium cyanide as the central ligand.

**Supplementary Materials:** The following supplementary information can be downloaded at: <https://www.mdpi.com/article/10.3390/catal12101136/s1>, Table S1: FAOR activity comparisons of RuPd<sub>3</sub> ANs with the previous reported catalysts [2,10,11,29,30,44,49–61]; Scheme S1: Graphical abstract; Figure S1: Photographs of Pd<sub>x</sub>[Ru(CN)<sub>6</sub>]<sub>y</sub>·aH<sub>2</sub>O cyanogels; Figure S2: The plot of lattice parameter versus Pd atomic percentage of RuPd<sub>3</sub> ANs; Figure S3: The EDS spectrum of (a) RuPd, (b) RuPd<sub>2</sub> and (c) RuPd<sub>3</sub> ANs, respectively; Figure S4: The XPS survey of RuPd<sub>3</sub> ANs; Figure S5: The large-scale SEM images of RuPd<sub>3</sub> ANs; Figure S6: (a) N<sub>2</sub> adsorption-desorption isotherms and (b) Brunauer–Emmett–Teller (BET) pore calculation of RuPd<sub>3</sub> ANs; Figure S7: Cyclic voltammetry curves of RuPd<sub>3</sub> ANs, RuPd<sub>2</sub>, RuPd and Pd black in 0.5 M H<sub>2</sub>SO<sub>4</sub> solution; Figure S8: Nyquist curves of RuPd<sub>3</sub> ANs and Pd Black in 0.5 M H<sub>2</sub>SO<sub>4</sub> + 0.5 M HCOOH electrolyte; Figure S9: Chronoamperometric curves obtained at 0.6 V (vs. RHE) in N<sub>2</sub>-saturated 0.5 M H<sub>2</sub>SO<sub>4</sub> + 0.5 M HCOOH solution; Figure S10: The 1st, 60th and 200th FAOR curves for accelerated durability tests (ADTs) tests in N<sub>2</sub>-saturated 0.5 M H<sub>2</sub>SO<sub>4</sub> + 0.5 M HCOOH solution, compared with (a) RuPd<sub>3</sub> ANs and (b) Pd black; Figure S11: The TEM image of RuPd<sub>3</sub> ANs after 200 cycles ADTs test.

**Author Contributions:** Conceptualization, Q.L., J.Z., D.S. and Y.T.; Synthesis and preparation of catalysts, Q.L., W.Y., J.Z. and Y.R.; Characterization, Q.L., W.Y., J.L. and X.Z.; writing—original draft, Q.L.; writing—review and editing, Q.L., D.S. and Y.T.; funding acquisition, Q.L. and Y.T. All authors have read and agreed to the published version of the manuscript.

**Funding:** We acknowledge the financial support from the National Natural Science Foundation of China (Grant No. 21875112 and Grant No. 22072067), the Natural Science Foundation of Jiangsu Province (Grant No. BK20171473) and the Postgraduate Research & Practice Innovation Program of Jiangsu Province (KYCX22\_1551). The authors also thank the support from the National and Local Joint Engineering Research Centre of Biomedical Functional Materials, a project sponsored by the Priority Academic Program Development of Jiangsu Higher Education Institutions.

**Data Availability Statement:** Not applicable.

**Acknowledgments:** We acknowledge the suggestions made by Gengtao Fu, Zhijuan Li and Chuang Fan for this work, and Mingxing Gong for his support in HRTEM technology, as well as Anzhou Yang for his support in the graphical abstract.

**Conflicts of Interest:** There are no conflict of interest to declare.

## References

1. Lv, F.; Zhang, W.; Sun, M.; Lin, F.; Wu, T.; Zhou, P.; Yang, W.; Gao, P.; Huang, B.; Guo, S. Au Clusters on Pd Nanosheets Selectively Switch the Pathway of Ethanol Electrooxidation: Amorphous/Crystalline Interface Matters. *Adv. Energy Mater.* **2021**, *11*, 2100187. [[CrossRef](#)]
2. Yang, L.; Li, G.; Chang, J.; Ge, J.; Liu, C.; Vladimir, F.; Wang, G.; Jin, Z.; Xing, W. Sea urchin-like Au@Pd shell electrocatalysts with high FAOR performance: Coefficient of lattice strain and electrochemical surface area. *Appl. Catal. B* **2020**, *260*, 118200. [[CrossRef](#)]
3. Feng, L.; Cui, Z.; Yan, L.; Xing, W.; Liu, C. The enhancement effect of MoO<sub>x</sub> on Pd/C catalyst for the electrooxidation of formic acid. *Electrochim. Acta* **2011**, *56*, 2051–2056. [[CrossRef](#)]
4. Zhang, J.; Wu, L.; Xu, L.; Sun, D.; Sun, H.; Tang, Y. Recent advances in phosphorus containing noble metal electrocatalysts for direct liquid fuel cells. *Nanoscale* **2021**, *13*, 16052–16069. [[CrossRef](#)] [[PubMed](#)]
5. Jiao, K.; Xuan, J.; Du, Q.; Bao, Z.; Xie, B.; Wang, B.; Zhao, Y.; Fan, L.; Wang, H.; Hou, Z.; et al. Designing the next generation of proton-exchange membrane fuel cells. *Nature* **2021**, *595*, 361–369. [[CrossRef](#)]
6. Wang, T.; Jiang, Y.; He, J.; Li, F.; Ding, Y.; Chen, P.; Chen, Y. Porous palladium phosphide nanotubes for formic acid electrooxidation. *Carbon Energy* **2022**, *4*, 283–293. [[CrossRef](#)]
7. Wang, Y.; Jiang, X.; Fu, G.; Li, Y.; Tang, Y.; Lee, J.; Tang, Y. Cu<sub>5</sub>Pt Dodecahedra with Low-Pt Content: Facile Synthesis and Outstanding Formic Acid Electrooxidation. *ACS Appl. Mater. Interfaces* **2019**, *11*, 34869–34877. [[CrossRef](#)] [[PubMed](#)]
8. Meng, Q.; Yang, X.; Wang, X.; Xiao, M.; Li, K.; Jin, Z.; Ge, J.; Liu, C.; Xing, W. Preparation Strategy Using Pre-Nucleation Coupled with In Situ Reduction for a High-Performance Catalyst towards Selective Hydrogen Production from Formic Acid. *Catalysts* **2022**, *12*, 325. [[CrossRef](#)]
9. Ma, Z.; Legrand, U.; Pahija, E.; Tavares, J.R.; Boffito, D.C. From CO<sub>2</sub> to Formic Acid Fuel Cells. *Ind. Eng. Chem. Res.* **2020**, *60*, 803–815. [[CrossRef](#)]
10. Hossain, S.K.S.; Alwi, M.M.; Saleem, J.; Al-Hashem, H.T.; McKay, G.; Mansour, S.; Ali, S.S. Bimetallic Pd-Co Nanoparticles Supported on Nitrogen-Doped Reduced Graphene Oxide as Efficient Electrocatalysts for Formic Acid Electrooxidation. *Catalysts* **2021**, *11*, 910. [[CrossRef](#)]
11. Teng, Z.; Li, M.; Li, Z.; Liu, Z.; Fu, G.; Tang, Y. Facile synthesis of channel-rich ultrathin palladium-silver nanosheets for highly efficient formic acid electrooxidation. *Mater. Today Energy* **2021**, *19*, 100596. [[CrossRef](#)]
12. Fang, Z.; Chen, W. Recent advances in formic acid electro-oxidation: From the fundamental mechanism to electrocatalysts. *Nanoscale Adv.* **2021**, *3*, 94–105. [[CrossRef](#)] [[PubMed](#)]
13. Rettenmaier, C.; Aran-Ais, R.; Timoshenko, J.; Rizo, R.; Jeon, H.; Kuhl, S.; Chee, S.; Bergmann, A.; Cuenya, B.R. Enhanced Formic Acid Oxidation over SnO<sub>2</sub>-decorated Pd Nanocubes. *ACS Catal.* **2020**, *10*, 14540–14551. [[CrossRef](#)] [[PubMed](#)]
14. Chang, J.; Feng, L.; Liu, C.; Xing, W.; Hu, X. An effective Pd-Ni<sub>(2)</sub>P/C anode catalyst for direct formic acid fuel cells. *Angew. Chem. Int. Ed.* **2014**, *53*, 122–126. [[CrossRef](#)]
15. Bhaskaran, R.; Abraham, B.G.; Chetty, R. Recent advances in electrocatalysts, mechanism, and cell architecture for direct formic acid fuel cells. *WIREs Energy Environ.* **2021**, *11*, e419. [[CrossRef](#)]
16. Liu, Q.; Wang, J.; Zhang, J.; Yan, Y.; Qiu, X.; Wei, S.; Tang, Y. In situ immobilization of isolated Pd single-atoms on graphene by employing amino-functionalized rigid molecules and their prominent catalytic performance. *Catal. Sci. Technol.* **2020**, *10*, 450–457. [[CrossRef](#)]
17. Chen, D.; Pei, S.; He, Z.; Shao, H.; Wang, J.; Wang, K.; Wang, Y.; Jin, Y. High Active PdSn Binary Alloyed Catalysts Supported on B and N Codoped Graphene for Formic Acid Electro-Oxidation. *Catalysts* **2020**, *10*, 751. [[CrossRef](#)]

18. Jiang, X.; Xiong, Y.; Wang, Y.; Wang, J.; Li, N.; Zhou, J.; Fu, G.; Sun, D.; Tang, Y. Treelike two-level Pd<sub>x</sub>Ag<sub>y</sub> nanocrystals tailored for bifunctional fuel cell electrocatalysis. *J. Mater. Chem. A* **2019**, *7*, 5248–5257. [[CrossRef](#)]
19. Xia, B.; Wu, H.; Yan, Y.; Wang, H.; Wang, X. One-pot synthesis of platinum nanocubes on reduced graphene oxide with enhanced electrocatalytic activity. *Small* **2014**, *10*, 2336–2339. [[CrossRef](#)]
20. Ye, S.; Feng, J.; Li, G. Pd Nanoparticle/CoP Nanosheet Hybrids: Highly Electroactive and Durable Catalysts for Ethanol Electrooxidation. *ACS Catal.* **2016**, *6*, 7962–7969. [[CrossRef](#)]
21. Peng, L.; Wei, Z. Catalyst Engineering for Electrochemical Energy Conversion from Water to Water: Water Electrolysis and the Hydrogen Fuel Cell. *Engineering* **2020**, *6*, 653–679. [[CrossRef](#)]
22. Yu, H.; Zhou, T.; Wang, Z.; Xu, Y.; Li, X.; Wang, L.; Wang, H. Defect-Rich Porous Palladium Metallene for Enhanced Alkaline Oxygen Reduction Electrocatalysis. *Angew. Chem. Int. Ed.* **2021**, *60*, 12027–12031. [[CrossRef](#)] [[PubMed](#)]
23. Zhang, L.; Wang, F.; Wang, S.; Huang, H.; Meng, X.; Ouyang, Y.; Yuan, W.; Guo, C.; Li, C. Layered and Heterostructured Pd/PdWCr Sheet-Assembled Nanoflowers as Highly Active and Stable Electrocatalysts for Formic Acid Oxidation. *Adv. Funct. Mater.* **2020**, *30*, 2003933. [[CrossRef](#)]
24. Xia, B.; Chen, Y. Preface to special issue on electrocatalysis for sustainable energy. *Chin. J. Catal.* **2022**, *43*, 1379. [[CrossRef](#)]
25. Wang, X.; Tang, Y.; Lee, J.; Fu, G. Recent advances in rare-earth-based materials for electrocatalysis. *Chem. Catal.* **2022**, *2*, 967–1008. [[CrossRef](#)]
26. Wang, X.; Zhu, Y.; Li, H.; Lee, M.; Tang, Y.; Fu, G. Rare-Earth Single-Atom Catalysts: A New Frontier in Photo/Electrocatalysis. *Small Methods* **2022**, *6*, 2200413. [[CrossRef](#)]
27. Wang, X.; Wang, J.; Wang, P.; Li, L.; Zhang, X.; Sun, D.; Li, Y.; Tang, Y.; Wang, Y.; Fu, G. Engineering 3d-2p-4f Gradient Orbital Coupling to Enhance Electrocatalytic Oxygen Reduction. *Adv. Mater.* **2022**, 2206540. [[CrossRef](#)]
28. Cao, K.; Yang, H.; Bai, S.; Xu, Y.; Yang, C.; Wu, Y.; Xie, M.; Cheng, T.; Shao, Q.; Huang, X. Efficient Direct H<sub>2</sub>O<sub>2</sub> Synthesis Enabled by PdPb Nanorings via Inhibiting the O–O Bond Cleavage in O<sub>2</sub> and H<sub>2</sub>O<sub>2</sub>. *ACS Catal.* **2021**, *11*, 1106–1118. [[CrossRef](#)]
29. Yan, X.; Hu, X.; Fu, G.; Xu, L.; Lee, J.; Tang, Y. Facile Synthesis of Porous Pd<sub>3</sub>Pt Half-Shells with Rich “Active Sites” as Efficient Catalysts for Formic Acid Oxidation. *Small* **2018**, *14*, e1703940. [[CrossRef](#)]
30. Liu, S.; Wang, Z.; Zhang, H.; Yin, S.; Xu, Y.; Li, X.; Wang, L.; Wang, H. B-Doped PdRu nanopillar assemblies for enhanced formic acid oxidation electrocatalysis. *Nanoscale* **2020**, *12*, 19159–19164. [[CrossRef](#)]
31. Ren, J.; Yao, Y.; Yuan, Z. Fabrication strategies of porous precious-metal-free bifunctional electrocatalysts for overall water splitting: Recent advances. *Green Energy Environ.* **2021**, *6*, 620–643. [[CrossRef](#)]
32. Li, Z.; Li, M.; Wang, X.; Fu, G.; Tang, Y. The use of amino-based functional molecules for the controllable synthesis of noble-metal nanocrystals: A minireview. *Nanoscale Adv.* **2021**, *3*, 1813–1829. [[CrossRef](#)]
33. Zaman, S.; Tian, X.; Su, Y.; Cai, W.; Yan, Y.; Qi, R.; Douka, A.; Chen, S.; You, B.; Liu, H.; et al. Direct integration of ultralow-platinum alloy into nanocarbon architectures for efficient oxygen reduction in fuel cells. *Sci. Bull.* **2021**, *66*, 2207–2216. [[CrossRef](#)]
34. Zhang, H.; Wang, H.; Xu, Y.; Zhuo, S.; Yu, Y.; Zhang, B. Conversion of Sb<sub>2</sub>Te<sub>3</sub> hexagonal nanoplates into three-dimensional porous single-crystal-like network-structured Te plates using oxygen and tartaric acid. *Angew. Chem. Int. Ed.* **2012**, *51*, 1459–1463. [[CrossRef](#)] [[PubMed](#)]
35. Wang, D.; Jiang, X.; Lin, Z.; Zeng, X.; Zhu, Y.; Wang, Y.; Gong, M.; Tang, Y.; Fu, G. Ethanol-Induced Hydrogen Insertion in Ultrafine IrPdH Boosts pH-Universal Hydrogen Evolution. *Small* **2022**, *18*, 2204063. [[CrossRef](#)]
36. Lin, S.; Yao, Y.; Zhang, L.; Feng, J.; Wang, J. Cyanogel and its derived-materials: Properties, preparation methods, and electrochemical applications. *Mater. Today Energy* **2021**, *20*, 100701. [[CrossRef](#)]
37. Wan, J.; Liu, Z.; Yang, X.; Cheng, P.; Yan, C. Cyanogel-Derived Synthesis of Porous PdFe Nanohydrangeas as Electrocatalysts for Oxygen Reduction Reaction. *Nanomaterials* **2021**, *11*, 3382. [[CrossRef](#)]
38. Burgess, C.M.; Yao, N.; Bocarsly, A.B. Stabilizing cyanosols: Amorphous cyanide bridged transition metal polymer nanoparticles. *J. Mater. Chem.* **2009**, *19*, 8846–8855. [[CrossRef](#)]
39. Liu, X.; Xu, G.; Chen, Y.; Lu, T.; Tang, Y.; Xing, W. A strategy for fabricating porous PdNi@Pt core-shell nanostructures and their enhanced activity and durability for the methanol electrooxidation. *Sci. Rep.* **2015**, *5*, 7619. [[CrossRef](#)]
40. Liu, H.; Liu, X.; Li, Y.; Jia, Y.; Tang, Y.; Chen, Y. Hollow PtNi alloy nanospheres with enhanced activity and methanol tolerance for the oxygen reduction reaction. *Nano Res.* **2016**, *9*, 3494–3503. [[CrossRef](#)]
41. Liu, Z.; Yang, X.; Cui, L.; Shi, Z.; Lu, B.; Guo, X.; Zhang, J.; Xu, L.; Tang, Y.; Xiang, Y. High-Performance Oxygen Reduction Electrocatalysis Enabled by 3D PdNi Nanocorals with Hierarchical Porosity. *Part. Part. Syst. Charact.* **2018**, *35*, 1700366. [[CrossRef](#)]
42. Bai, J.; Xue, Q.; Zhao, Y.; Jiang, J.; Zeng, J.; Yin, S.; Chen, Y. Component-Dependent Electrocatalytic Activity of Ultrathin PdRh Alloy Nanocrystals for the Formate Oxidation Reaction. *ACS Sustain. Chem. Eng.* **2018**, *7*, 2830–2836. [[CrossRef](#)]
43. Liu, X.; Zhang, Y.; Gong, M.; Tang, Y.; Lu, T.; Chen, Y.; Lee, J. Facile synthesis of corallite-like Pt–Pd alloy nanostructures and their enhanced catalytic activity and stability for ethanol oxidation. *J. Mater. Chem. A* **2014**, *2*, 13840–13844. [[CrossRef](#)]
44. Liu, Q.; Li, Z.; Zhou, X.; Xiao, J.; Han, Z.; Jiang, X.; Fu, G.; Tang, Y. Cyanogel-Induced PdCu Alloy with Pd-Enriched Surface for Formic Acid Oxidation and Oxygen Reduction. *Adv. Energy Sustain. Res.* **2022**, 2200067. [[CrossRef](#)]
45. Liu, Z.; Yang, X.; Lu, B.; Shi, Z.; Sun, D.; Xu, L.; Tang, Y.; Sun, S. Delicate topotactic conversion of coordination polymers to Pd porous nanosheets for high-efficiency electrocatalysis. *Appl. Catal. B* **2019**, *243*, 86–93. [[CrossRef](#)]
46. Shi, H.; Fang, Z.; Zhang, X.; Li, F.; Tang, Y.; Zhou, Y.; Wu, P.; Yu, G. Double-Network Nanostructured Hydrogel-Derived Ultrafine Sn-Fe Alloy in Three-Dimensional Carbon Framework for Enhanced Lithium Storage. *Nano Lett.* **2018**, *18*, 3193–3198. [[CrossRef](#)]

47. Liu, H.; Li, J.; Wang, L.; Tang, Y.; Xia, B.Y.; Chen, Y. Trimetallic PtRhNi alloy nanoassemblies as highly active electrocatalyst for ethanol electrooxidation. *Nano Res.* **2017**, *10*, 3324–3332. [[CrossRef](#)]
48. Ahmad, A.; Khan, S.; Tariq, S.; Luque, R.; Verpoort, F. Self-sacrifice MOFs for heterogeneous catalysis: Synthesis mechanisms and future perspectives. *Mater. Today* **2022**, *55*, 137–169. [[CrossRef](#)]
49. Zhang, H.; Cen, K.; Wen, J.; Qi, M.; Ge, X.; Liu, Y.; Sun, D.; Tang, Y. One-Pot Synthesis of Porous Palladium Nanorods for Efficient Formic Acid Electro-Oxidation Reaction. *Sci. Adv. Mater.* **2017**, *10*, 460–466. [[CrossRef](#)]
50. Zhang, L.; Sui, Q.; Tang, T.; Chen, Y.; Zhou, Y.; Tang, Y.; Lu, T. Surfactant-free palladium nanodendrite assemblies with enhanced electrocatalytic performance for formic acid oxidation. *Electrochem. Commun.* **2013**, *32*, 43–46. [[CrossRef](#)]
51. Qiu, X.; Zhang, H.; Dai, Y.; Zhang, F.; Wu, P.; Wu, P.; Tang, Y. Sacrificial Template-Based Synthesis of Unified Hollow Porous Palladium Nanospheres for Formic Acid Electro-Oxidation. *Catalysts* **2015**, *5*, 992–1002. [[CrossRef](#)]
52. Qiu, X.; Zhang, H.; Wu, P.; Zhang, F.; Wei, S.; Sun, D.; Xu, L.; Tang, Y. One-Pot Synthesis of Freestanding Porous Palladium Nanosheets as Highly Efficient Electrocatalysts for Formic Acid Oxidation. *Adv. Funct. Mater.* **2017**, *27*, 1603852. [[CrossRef](#)]
53. Xu, L.; Wang, K.; Yuan, Q. One-pot synthesis of lotus-shaped Pd–Cu hierarchical superstructure crystals for formic acid oxidation. *RSC Adv.* **2016**, *6*, 96079–96083. [[CrossRef](#)]
54. Xu, J.; Zhao, M.; Yamaura, S.-I.; Jin, T.; Asao, N. Core-shell Pd–P@Pt nanoparticles as efficient catalysts for electrooxidation of formic acid. *J. Appl. Electrochem.* **2016**, *46*, 1109–1118. [[CrossRef](#)]
55. Wang, H.; Li, Y.; Li, C.; Wang, Z.; Xu, Y.; Li, X.; Xue, H.; Wang, L. Hyperbranched PdRu nanospine assemblies: An efficient electrocatalyst for formic acid oxidation. *J. Mater. Chem. A* **2018**, *6*, 17514–17518. [[CrossRef](#)]
56. Yang, F.; Zhang, Y.; Liu, P.-F.; Cui, Y.; Ge, X.-R.; Jing, Q.-S. Pd–Cu alloy with hierarchical network structure as enhanced electrocatalysts for formic acid oxidation. *Int. J. Hydrogen Energy* **2016**, *41*, 6773–6780. [[CrossRef](#)]
57. Shen, T.; Chen, S.; Zeng, R.; Gong, M.; Zhao, T.; Lu, Y.; Liu, X.; Xiao, D.; Yang, Y.; Hu, J.; et al. Tailoring the Antipoisoning Performance of Pd for Formic Acid Electrooxidation via an Ordered PdBi Intermetallic. *ACS Catal.* **2020**, *10*, 9977–9985. [[CrossRef](#)]
58. Yang, G.; Chen, Y.; Zhou, Y.; Tang, Y.; Lu, T. Preparation of carbon supported Pd–P catalyst with high content of element phosphorus and its electrocatalytic performance for formic acid oxidation. *Electrochem. Commun.* **2010**, *12*, 492–495. [[CrossRef](#)]
59. Shen, T.; Lu, Y.; Gong, M.; Zhao, T.; Hu, Y.; Wang, D. Optimizing Formic Acid Electro-oxidation Performance by Restricting the Continuous Pd Sites in Pd–Sn Nanocatalysts. *ACS Sustain. Chem. Eng.* **2020**, *8*, 12239–12247. [[CrossRef](#)]
60. Xu, Y.; Yu, S.; Ren, T.; Li, C.; Yin, S.; Wang, Z.; Li, X.; Wang, L.; Wang, H. A quaternary metal–metalloid–nonmetal electrocatalyst: B, P-co-doping into PdRu nanospine assemblies boosts the electrocatalytic capability toward formic acid oxidation. *J. Mater. Chem. A* **2020**, *8*, 2424–2429. [[CrossRef](#)]
61. Goswami, C.; Saikia, H.; Tada, K.; Tanaka, S.; Sudarsanam, P.; Bhargava, S.K.; Bharali, P. Bimetallic Palladium–Nickel Nanoparticles Anchored on Carbon as High-Performance Electrocatalysts for Oxygen Reduction and Formic Acid Oxidation Reactions. *ACS Appl. Energy Mater.* **2020**, *3*, 9285–9295. [[CrossRef](#)]